

Optical matrix imaging applied to embryology

Victor Barolle,^{1,*} Flavien Bureau,^{1,*} Nicolas Guigui,¹ Paul Balondrade,¹ Vincent Brochard,² Olivier Dubois,² Alice Jouneau,² Amélie Bonnet-Garnier,² and Alexandre Aubry^{1,†}

¹*PSL University, ESPCI Paris, CNRS,
Institut Langevin, Paris, France*

²*INRAE, BREED, Jouy-en-Josas, France*

(Dated: October 16, 2024)

Abstract

High-resolution label-free imaging of oocytes and embryos is essential for *in vitro* fertilization procedures. Yet conventional microscopy fails in this task because of aberrations and multiple scattering induced by refractive index heterogeneities inside the sample. These detrimental phenomena drastically degrade the images of early embryos particularly in depth. To overcome these fundamental problems without sacrificing the frame rate, optical matrix imaging (OMI) is a suitable tool. Relying on an ultra-fast measurement of the reflection matrix associated with the sample, it can compensate for aberration and forward multiple scattering in post-processing, thereby providing three-dimensional and highly contrasted images of embryos at a confocal resolution. As a first proof-of-concept, bovine oocytes and embryos are imaged at a 300 nm resolution almost in real time. Our system enables visualization of intracellular structures such as lipids and mitochondria in the cytoplasm or the zona pellucida surrounding it. Altogether, we demonstrate that OMI is a promising tool for research in developmental biology and for time-lapse monitoring of oocytes and embryos in assisted reproduction.

* These authors equally contributed to this work

† Corresponding author: alexandre.aubry@espci.fr

INTRODUCTION

Embryo imaging plays a crucial role in In-Vitro Fertilization (IVF) procedures today. It is used to assess key morphological criteria [1] that form the basis for evaluating an embryo’s development potential and guiding decisions on whether to transfer or freeze the embryo. However, current non-invasive imaging techniques are limited to phase contrast microscopes [2], that only give access to two-dimensional, shallow in depth images, and lack quantitative data. Bright-field microscopy struggles to image embryos in depth because of two major physical challenges that degrade image contrast and resolution: aberrations [3] and multiple scattering [4].

The standard for 3D biological imaging is confocal imaging using fluorescent labelling. A recent study [5] has shown for instance how to exploit fluorescent dyes to study chromosome dynamics during embryo development. However, this approach is invasive and cannot be used, in daily practice, in clinics. Optical coherence microscopy [6] is a promising label-free imaging technique, but is limited in depth and the acquisition is too slow to be used in the clinic. Nevertheless, it was used, in a recent work [7], to count the number of nuclei in an embryo and showed it was correlated to the development to blastocyst. Interestingly, full-field OCT has also been lately used to study nucleolus in germinal vesicle stage mouse oocytes and intracellular dynamics during embryo development [8]. Although the obtained images are spectacular, they remain impacted by aberrations and rely on an axial scan of the sample for 3D imaging, which limits both the image quality and the frame rate.

To solve the fundamental problem of aberrations, adaptive focusing was introduced years ago in astronomy to compensate for phase distortions undergone by starlight when it passes through the atmosphere [9–12]. Adaptive optics was then transposed to optical microscopy in the 2000s along with the development of deformable mirrors with increasing number of elements [13–15]. However, this is at the price of a more complex set up and a much longer acquisition scheme. For deep imaging and to circumvent multiple scattering, a complex spatio-temporal focusing law should ideally be tailored for each voxel of the medium, which is prohibitive for real-life applications.

Inspired by previous ultrasound studies [16, 17] and computational adaptive optics [18, 19], a reflection matrix approach of optical microscopy, that we will refer to as optical matrix imaging (OMI), has been developed to overcome these difficulties [20–22]. It consists in acquiring the reflection matrix associated with the medium to be imaged by illuminating the sample by a set of incident waves and recording the corresponding back-scattered wave-fields *via* interferometry. Once recorded, this reflection matrix contains all the information available on the medium. In particular, because of the linearity of the wave equation and its time reversal symmetry, it can be used to simulate wave focusing in post-processing

and iterate the process until reaching local adaptive focusing laws for each medium voxel [23].

Technically the reflection matrix can be acquired using various illumination and detection schemes [20, 24–30] but the measurement time remained prohibitive for real-time applications until recently. However, in a recent study [31, 32], this bottleneck has been circumvented by the use of a wavelength swept source, a sparse illumination sequence and a detection scheme based on on-axis holography and an ultra-fast camera. This device is fully compatible with in-vitro and in-vivo applications. The acquisition of this large amount of data is very fast (1.8 Gb/s) and provides 3D non-invasive real-time microscopic imaging. The recorded reflection matrix is post-processed with focusing and aberration correction algorithms to retrieve a confocal resolution. A digital clearing of refractive index heterogeneities is thus applied and a 3D image of the sample is obtained with an optimized contrast and close-to-ideal resolution throughout the volume.

The first experimental proof-of-concept has been performed on an opaque cornea [31]. However, this device is not restricted to ophthalmic applications and the goal of this paper is to show its potential interest for embryology. To that aim, the setup proposed in Ref. [31] is converted to an inverted configuration in order to allow for non-invasive imaging of bovine oocytes and embryos directly on a dish. We then demonstrate the interest of OMI for this application. In particular, we will show: (i) OMI can be used to quantify aberrations and multiple scattering phenomena in embryos; (ii) OMI can exploit the speckle generated by the random distribution of lipids in cells to tailor complex focusing laws; (iii) OMI can leverage these focusing laws to reach a sub-micron resolution over the whole embryo volume at different steps of their development; (iv) OMI can produce quantitative information on embryos by performing the segmentation of cells and their nuclei.

RESULTS

Recording the reflection matrix

The experimental setup has already been described in Ref. [31]. It consists of a Linnik interferometer with the two identical microscope objectives (MO, NA=0.75) in the sample and reference arms. The experimental procedure is detailed in Methods. In a few words, the sample is illuminated through a MO by a set of plane waves (Fig. 1b) at different wavelengths in the 800 – 875 nm-range (Fig. 1a). To that aim, the incident beam is focused on the MO pupil planes. Each pupil is scanned according to a predefined sequence to produce a set of incident plane waves (Methods) that result in a full-field illumination on the sample and the reference mirror. The back-scattered fields are collected by the same MOs and their interferogram is recorded by an ultra-fast camera conjugated with the MOs’ focal plane. Each wave-field reflected by the sample

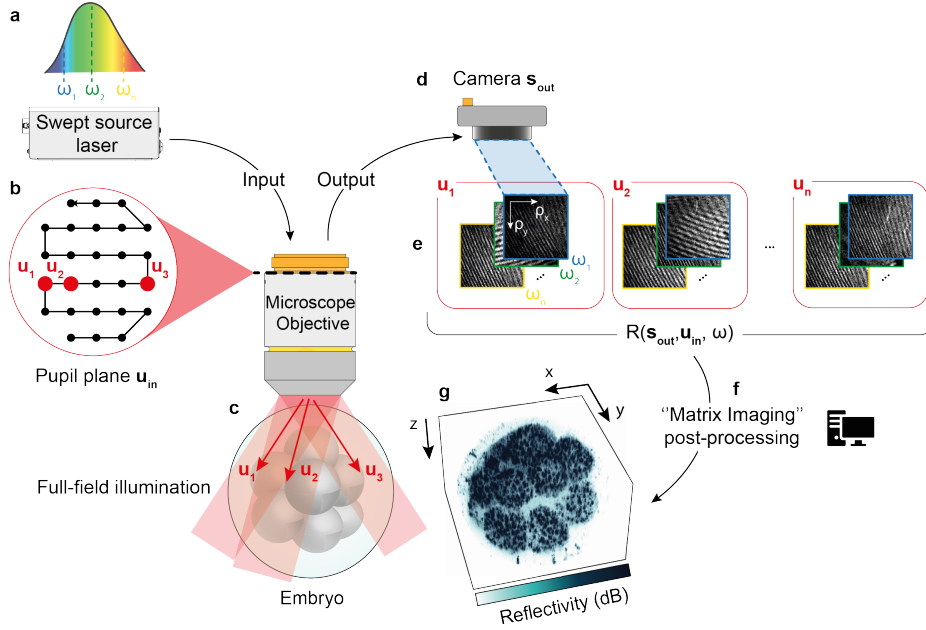


Figure 1. **Imaging set-up.** **a-b**, A swept source laser (**a**) is focused at successive points \mathbf{u}_{in} in the MO pupil plane (**b**). **c**, Each point in the pupil plane is associated with a plane-wave that gives rise to a full-field illumination of the sample. **d**, For each wavelength and each plane-wave, reflected wavefronts are recorded on a camera that is conjugated with a plane located inside the sample. A reference arm that is not displayed in this figure for simplification allows the recording of an interferogram. **e**, All this wealth of information is stored into the reflection matrix \mathbf{R} . **f**, Post-processing operations referred to as “Matrix Imaging” allow the compensation for aberrations and finally lead to an optimized volumetric image of the sample.

is extracted by means of on-axis holography and is noted $R(\mathbf{s}_{\text{out}}, \mathbf{u}_{\text{in}}, \omega)$, where \mathbf{s}_{out} are the pixel coordinates of the camera, \mathbf{u}_{in} accounts for the position of the input focusing beam in the MO pupil plane and ω stands for the incident light frequency. The whole set of reflected wave-fields are stored in the so-called reflection matrix $\mathbf{R}_{\text{su}}(\omega) = [R(\mathbf{s}_{\text{out}}, \mathbf{u}_{\text{in}}, \omega)]$. It gathers the information reflected by the sample for all the spatio-temporal degrees of freedom provided by the setup.

Focusing the reflection matrix

A numerical focusing of the reflection matrix is then performed at each depth z of the sample [31]. It consists in the application of Fresnel propagators at input and output of the reflection matrix to project the optical data at each depth z . An auto-focusing process is also applied to make the coherent volume and focusing

plane coincide. The result is a focused reflection matrix $\mathbf{R}_{\rho\rho}(z) = [R(\boldsymbol{\rho}_{\text{out}}, \boldsymbol{\rho}_{\text{in}}, z)]$ at each depth z that contains the time-gated responses between virtual sensors of expected positions $(\boldsymbol{\rho}_{\text{in}}, z)$ and $(\boldsymbol{\rho}_{\text{out}}, z)$.

A raw confocal image \mathbf{I}_C can be built by considering the diagonal elements of $\mathbf{R}_{\rho\rho}(z)$ ($\boldsymbol{\rho}_{\text{in}} = \boldsymbol{\rho}_{\text{out}}$):

$$I_C(\boldsymbol{\rho}, z) = R(\boldsymbol{\rho}, \boldsymbol{\rho}, z). \quad (1)$$

A transverse cross-section of the bovine oocyte is displayed in Fig 2b. The zona pellucida and a granular compartment inside the zona pellucida which corresponds to the cytoplasm of the oocyte can be distinguished. However, the image displays a highly blurred feature caused by the two fundamental problems we always have to cope with in optical microscopy, namely aberrations and multiple scattering. The aberrations are caused by the mismatch between the propagation model used in the post-processing scheme (homogeneous refractive index) and the real refractive index distribution inside the oocyte. The different structures in the oocyte exhibit different refractive index values, which distorts the point spread function of the OMI imaging system across the field-of-view and degrades the resolution and contrast of the confocal image. Multiple scattering is caused by short-scale heterogeneities that produce a speckle-like granularity inside the cytoplasm, but that also induce multiple scattering events. The latter phenomenon gives rise to the hazy texture of the confocal image.

Quantifying aberrations and multiple scattering

These detrimental phenomena can be quantified by extracting a local reflection point spread function (RPSF) from the focused reflection matrix [30, 31]. By scanning each virtual detector $\boldsymbol{\rho}_{\text{out}}$ with respect to each virtual source $\boldsymbol{\rho}_{\text{in}}$, one can actually probe the local focusing quality (Methods, Eq. 2). The result is a map of RPSFs across the field-of-view. One example is provided in Fig. 2d at the same depth as the image displayed in Fig. 2b. Each RPSF exhibits the following characteristic shape: a distorted and enlarged confocal spot due to aberrations on top of a diffuse background. While the latter component is due to multiple scattering, the former component contains the contribution of singly-scattered photons but also a coherent back-scattering peak resulting from a constructive interference between multiple scattering paths [30, 33].

The RPSF map shows important fluctuations due to: (i) the variations of the medium reflectivity that acts on the level of the confocal spot with respect to the diffuse background; (ii) the lateral variations of the optical index upstream of the focal plane that induce distortions of the confocal peak. Such complexity implies that any point in the medium will be associated with its own distinct focusing law. Nevertheless, spatial correlations subsist between RPSFs in adjacent windows (Fig. 2d). Such correlations can be explained by a physical phenomenon often referred to as isoplanatism in adaptive optics [12] and that results in a

locally-invariant PSF [34]. This local isoplanicity can be exploited for the estimation of local aberration phase laws $\phi(\mathbf{u}, \boldsymbol{\rho}, z)$ in the pupil plane (\mathbf{u}) for each medium voxel ($\boldsymbol{\rho}, z$).

Compensating for wave distortions

The estimation of these aberration phase laws is performed through an iterative phase reversal algorithm [23, 31] applied to the wave distortions [21] exhibited by the reflection matrix in the pupil plane. The result is displayed in Fig. 2a. The aberration phase laws $\phi(\mathbf{u}, \boldsymbol{\rho}, z)$ exhibit a concentric behavior due to the spherical shape of the oocyte. Most of the aberrations are thus due to the index mismatch between the oocyte and the surrounding liquid. These local aberration phase laws can be leveraged to estimate the transmission matrix between the imaging plane ($\boldsymbol{\rho}_{\text{in/out}}$) and each voxel ($\boldsymbol{\rho}, z$) of the oocyte (Methods, Eq. 3). The transmission matrices can be used to deconvolve the focused reflection matrix (Methods, Eq. 4). The associated confocal image (Methods, Eq. 5) is displayed in Fig. 2c. Compared to its initial counterpart (Fig. 2b), a drastic gain in terms of contrast and resolution is obtained. It now clearly highlights the different components of the oocyte: (i) the cytoplasm at the center, which displays a granular aspect and (ii) a thick girdle surrounding it, the so-called zona pellucida.

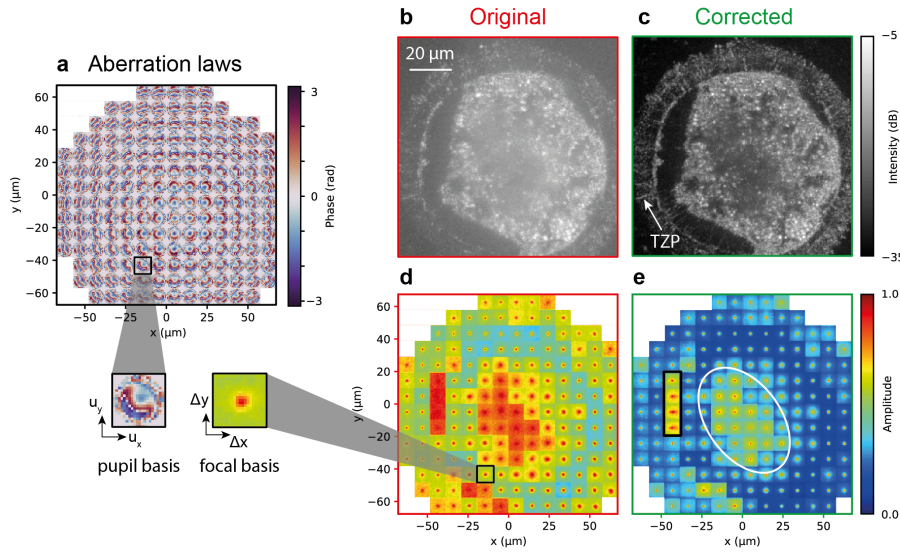


Figure 2. **Optical Matrix Imaging of an oocyte at depth $z = 64 \mu\text{m}$.** **a**, Aberration laws map. **b-c**, En-face images before and after the correction process, respectively. **d-e**, RPSF map before and after the correction process, respectively.

The benefit of OMI can be quantified by the associated map of RPSFs displayed

in Fig. 2e. Compared to their initial counterpart (Fig. 2d), the confocal peak now reaches the diffraction limit, $\delta\rho_c \sim \lambda/(4NA) \sim 290$ nm, almost everywhere, except in the area surrounded by a black rectangle associated with the perivitelline space of zero reflectivity (Fig. 2c). At the center of the oocyte (white ellipse), the RPSF displays a profile characteristic of multiple scattering with a confocal peak enhancement close to two that we attribute to the coherent back-scattering phenomenon [30, 33]. This indicates that the back-scattered photons from this region mainly arise from multiple scattering paths. It explains the blurred feature of the confocal image in that region, despite the aberration correction process. Everywhere else, the diffuse background is much lower than the confocal peak. The confocal signal mainly results from singly-scattered photons, and a contrasted image of the oocyte reflectivity is obtained in most of the field-of-view.

Origin of speckle in the cytoplasm

Oocytes images generated with OMI (Figure 2) allow us to identify the zona pellucida (ZP), the trans-zonal projections (TZP) [35] (white arrow in Fig. 2c) and a granular /bright compartment inside the zona pellucida which corresponds to the cytoplasm of the oocyte. To assess which components account for the granularity inside the oocyte, we centrifuged oocytes (Methods) before imaging them again. As in the previous experiment (Fig. 3a), the raw confocal image exhibits a weak contrast because of aberrations and multiple scattering (Fig. 3b₁, b₃). Once again, OMI compensates for those detrimental phenomena and provides a much more contrasted image of the centrifugated oocyte (Figs. 3b₂, b₄).

The centrifugation allows the segregation of the oocyte components according to their density. More precisely, histological light microscopy [36], epi-fluorescence microscopy [37] or bright field imaging (Fig. 4a) already showed that, upon centrifugation, the organelles stratify in five distinct zones according to their density: (i) lipids; (ii) membrane-bound vesicles; (iii) smooth endoplasmic reticulum; (iv) organelle-free ooplasm; and (v) mitochondria. The lipids are supposed to be concentrated at the centripetal pole while the dense mitochondria emerge on the other side at the centrifugal pole.

This centrifugation feature is nicely retrieved in Fig. 4b. Transverse cross-sections of the three-dimensional image (Figs. 3c) show the following segregation: (i) lipid droplets on the bottom left that give rise to an extremely bright speckle; (ii) on top of which is a less echogenic layer of membrane-bound vesicles; (iii) a clear zone corresponding to the organelle-free ooplasm and; (iv) mitochondria on the top right that also exhibit a strong reflectivity, albeit weaker than lipids.

This experiment thus sheds a new light onto the previous image of the oocyte displayed in Fig. 3a. In particular, the brightest spots in the cytoplasm can now be unambiguously assigned to lipids. Lipids are ubiquitous in bovine samples and usually hinder brightfield imaging, as shown by Fig. 4a. The discrimination

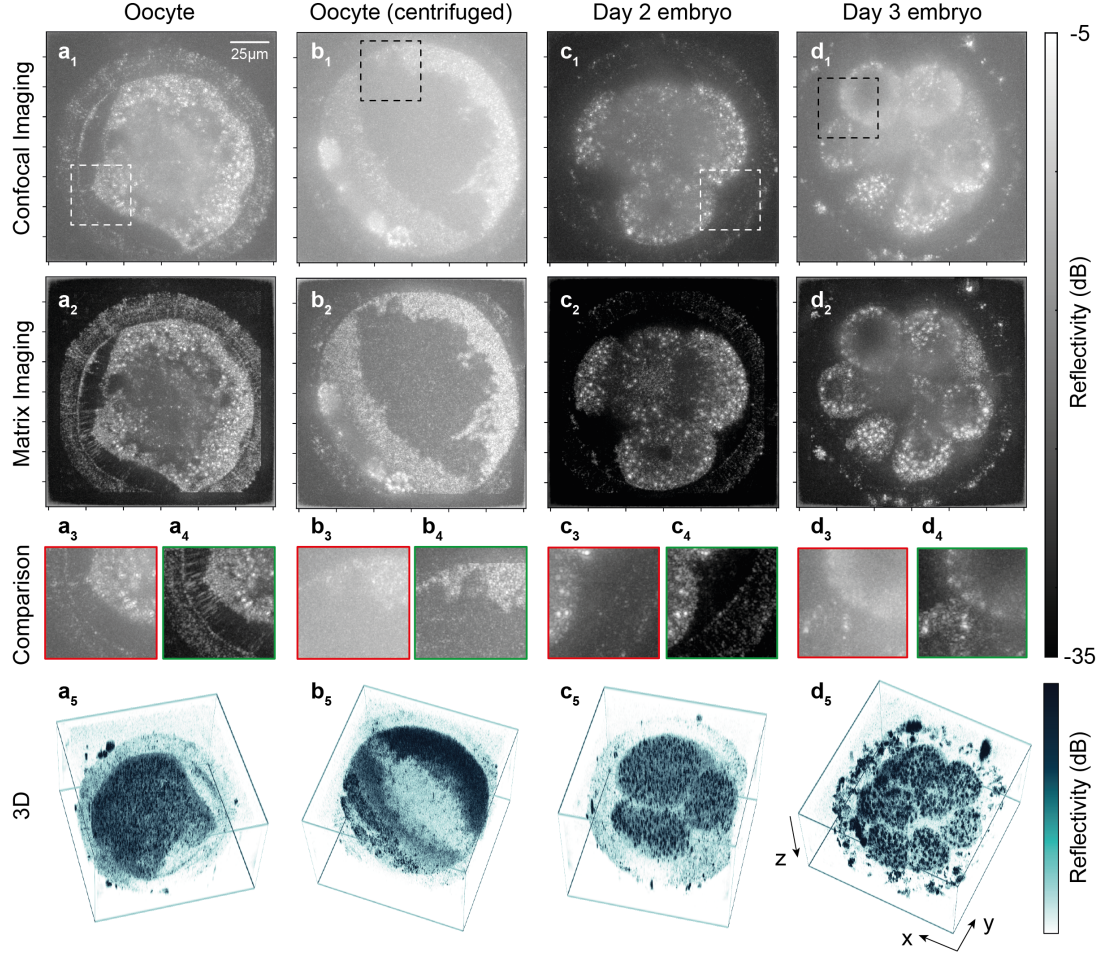


Figure 3. **Oocyte and embryo imaging.** **a**, Oocyte. **b**, Centrifuged oocyte. **c**, Day 2 embryo. **d**, Day 3 embryo. The first line of panels (subscript “1”) corresponds to the raw confocal image (Eq. 1). The second line of panels (subscript “2”) corresponds to the OMI image. The third line of panels (subscripts “3” and “4”) compares insets of the two first lines. The zoomed area is displayed with a dashed rectangle in the top panels. The last line (subscript “5”) shows a three-dimensional view of the OMI image displayed with a maximum intensity projection.

between mitochondria and membrane-bound vesicles is less obvious, with an observation only based on the reflectivity. However, in a near future, a dynamic contrast [8, 38] will also be provided by our ultra-fast imaging system. It will constitute a relevant observable to bring colors to reflectivity images and better appreciate the exact nature and behavior of each cytoplasm component.

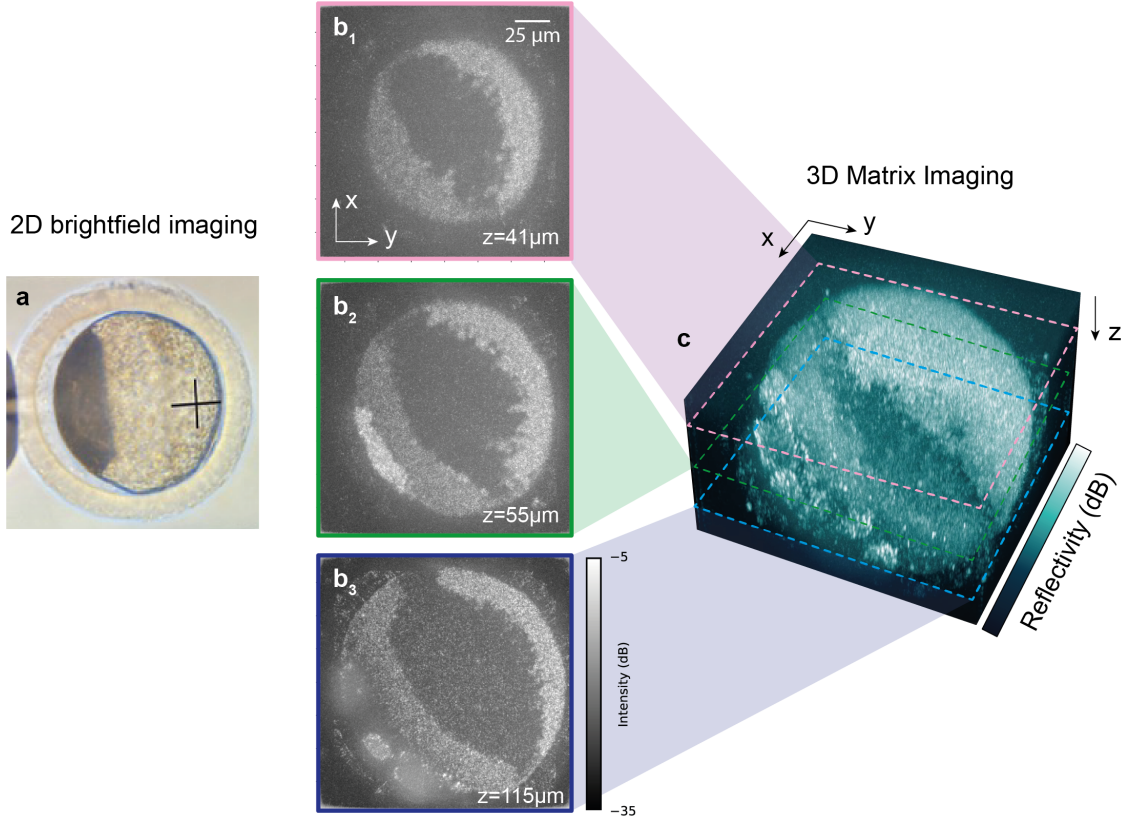


Figure 4. **Three-dimensional imaging of a centrifuged oocyte.** **a**, 2D bright-field image of a centrifuged oocyte using a conventional imaging system. **b**, **c** Cross-sections and 3D view of a different centrifuged oocyte using our imaging set-up. Subscripts “1”, “2” and “3” refer to depths $z = 41$, $z = 55$ and $z = 115 \mu\text{m}$, respectively.

Matrix imaging of embryos

OMI can also be an extremely powerful tool to monitor the development of embryos. As a first proof-of-concept, we performed imaging of two embryos at different stages of development: A day 2 (D2) embryo (Fig. 3c) and a day 3 (D3) embryo (Fig. 3d), respectively.

As for the oocyte, OMI manages to clear the fog exhibited by the raw confocal images (see comparison between Figs. 3c₁,c₂ and Figs. 3d₁,d₂). Figure 5b displays the map of aberration phase laws extracted by OMI in a longitudinal cross-section of the D2 embryo. While, at shallow depth, the aberration amounts to a simple defocus, their complexity drastically increases with depth. This large spatial frequency content exhibited by $\phi(\mathbf{u})$ in depth is characteristic of forward multiple scattering trajectories. The onset of multiple scattering is also highlighted by the

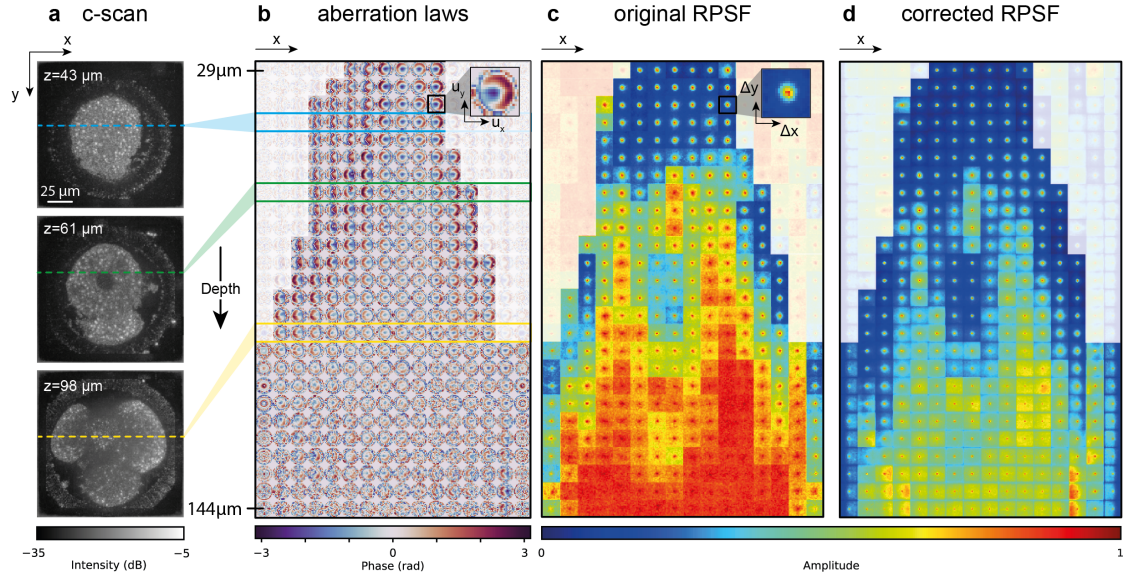


Figure 5. **Matrix imaging of a day 2 embryo.** **a**, En-face OMI images at three different depths. **b**, Map of aberration laws in a longitudinal (x, z)-plane. **c,d** RPSF map in the same plane, before and after aberration correction, respectively.

gradual increase of the diffuse background on the RPSFs (Figure 5b). Aberration compensation operated by OMI provides a confocal spot whose extension reaches the diffraction limit and a clear decrease of multiple scattering (Figure 5c). Nevertheless, the OMI process shows some limits with an RPSF that *a priori* still exhibits a profile characteristic of multiple scattering with a coherent backscattering enhancement of 2 at large depths. This explains the residual fog exhibited by the OMI image at large depths (see bottom panel of Fig. 5a). There is still some room for improving the OMI pipeline as it will be discussed further. Nevertheless, the obtained images are already of sufficient quality to provide a quantitative analysis of the embryos.

Towards quantitative imaging of embryos

As in the oocyte, lipid sparkling enables the clear distinction of each cell (named blastomere) in the embryos displayed in Figs. 3c and d. Strikingly, an anechoic inclusion is also clearly visible in the cytoplasm of each cell. As already revealed by previous works [6], these dark regions *a priori* correspond to cell nuclei. This characteristic feature will enable counting nuclei in an embryo up to the blastocyst stage. Being able to assess the number of cells and the number of nucleus in each cell will enable the detection of multinucleation and will provide valuable information about the embryo developmental potential [39].

Figure 6 shows the potential interest of such a segmentation for the D2 embryo. It enables the mapping of cell organization in space and its morphology with the evaluation of the size, shape/sphericity/compactness and volume of each cell. The presence of blastomeres of varying sizes may serve as an indicator of previous abnormal cell division, thereby representing a potential marker of embryo quality. In the present case, the segmentation of the 3D image (Fig. 6a) shows that the D2 embryo contains five cells (Fig. 6c). A similar process applied to D3 leads to a number of 11 cells. Note that an odd number of cells is not surprising here since cell divisions are asynchronous in bovine embryos [40].

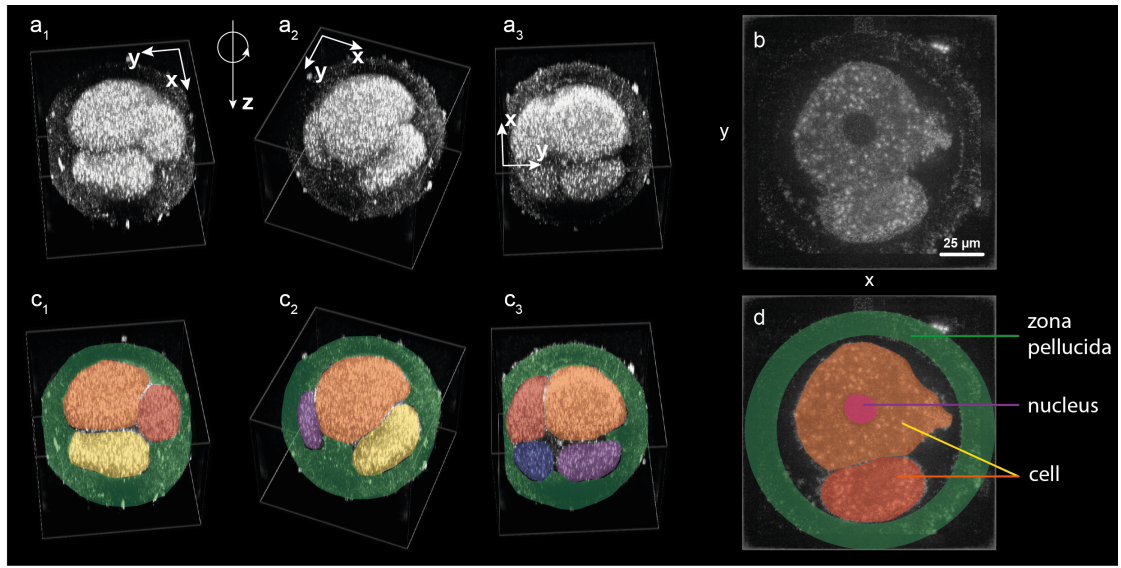


Figure 6. **Segmentation of the day 2 embryo.** a,c 3D view (maximum intensity projection) and its segmentation. b,d 2D cross-section at depth $z = 66 \mu\text{m}$ and its segmentation. Subscripts “1”, “2” and “3” stand for three different viewpoints.

DISCUSSION

Beyond cell segmentation, further works towards quantitative imaging will also consist in mapping physical parameters governing light propagation through embryos. The optical index [41] and the scattering mean free path [42] can actually be crucial bio-markers for a label-free characterization of embryos and their time-lapse monitoring [43]. For such measurements, matrix imaging will be a powerful tool as shown by recent works in ultrasound [44–46].

As shown by the RPSFs measured at the end of the OMI process (Figs. 2 and 5c), multiple scattering is still predominant at large depths and remain an hurdle for a contrasted image of embryos over their whole volume. Further efforts will

be needed in order to go beyond forward multiple scattering and harness more complex scattering trajectories. Interestingly, the multi-spectral reflection matrix gives access to temporal degrees of freedom that can be exploited for tailoring complex spatio-temporal focusing laws [29] required to overcome the diffusive limit.

To conclude, this study demonstrates the potential benefit of OMI for embryology. By providing a label-free three-dimensional image of oocytes and embryos in almost real-time, OMI surpasses concurrent methods such as optical coherence microscopy that only provides en-face image and still requires a mechanical scan of the sample for 3D imaging. Moreover, this study shows that a computational compensation of aberrations and forward multiple scattering is critical for a quantitative characterization of embryos. We therefore see OMI as an extremely promising tool for understanding the biological processes at work in embryo development and enhancing abilities to predict the viability of embryos before *in-utero* implantation in a IVF process.

METHODS

Sample preparation

Bovine ovaries were obtained from a local slaughterhouse and transported in NaCl solution 0.9% . Cumulus-oocyte complexes (COCs) were collected from each follicle and washed in Euroflush supplemented medium. A stringent selection of COCs was performed to eliminate defective ones before maturation. Subsequently, COCs were cultured for 22 hours in a maturation medium under specific atmospheric conditions (5% CO₂ and 38.5°C). After in vitro maturation (IVM), MII oocytes were washed with an in vitro fertilization (IVF) medium. Simultaneously, frozen semen was thawed and subjected to selection using density bovipure gradient centrifugation. Approximately 10⁶ sperm/ml were added to each drop containing matured oocytes in IVF medium. Following IVF for 22 hours at 5% CO₂ and 5% O₂ at 38.5°C, cumulus cells were removed by vortexing for 5 minutes, and putative zygotes were transferred to a drop of SOF (Syntetic Oviductal fluid) covered with oil and incubated at 5% CO₂ and 5% O₂ at 38.5°C for further development during 24 to 48 hours. D2 and D3 bovine embryos were fixed with 2% PFA (20 min at RT) prior transfer in a drop of PBS. The oocytes (after IVM and removal of the cumulus cells) were either centrifuged 7 min at 13400g or not before fixation in PFA 2% and imaging in a drop of PBS.

Experimental components

The following components were used in the experimental set-up already described in Ref. [31]: A swept laser source (800-875 nm; Superlum-850 HP), 1 galvanometer (Thorlabs, LSKGG4), 2 objective lenses (Olympus UPLFLN ×40; NA 0.75), and a 512×512 ultrafast camera (7 kHz; Phantom-710).

Reflection matrix acquisition

In each OMI experiment, 120 wavelengths in the $[800 - 875]$ nm range are scanned with the swept-source laser. At each wavelength, 325 incident plane waves were used to record the reflection matrix for the oocyte and the D3 embryo, while 425 illuminations were used for the centrifuged oocyte and the D2 embryo. Given the magnification of the imaging system and the inter-pixel distance of the camera ($\delta s = 20 \mu\text{m}$), the output wave field is sampled at a resolution close to $\lambda/(4NA)$, the theoretical achievable resolution for a confocal image: $\delta\rho_c = 300 \text{ nm}$.

Data acquisition and graphics processing unit processing

All the interferograms of the acquisition sequence are recorded by the camera in 6 s and streamed to the computer's RAM using Bitflow Cyton CXP frame grabbers. The numerical post-processing of the reflection matrix is performed by a graphics processing unit (NVIDIA RTX A6000). For the dataset considered in this paper, all the focusing and aberration correction algorithms are performed in 15 minutes.

Focused reflection matrix

The projection of the recorded reflection matrix into the focused basis is performed by applying, in post-processing, focusing operations described in Ref. [31]. It consists in the application of Fresnel operators by considering water (refractive index $n_0 = 1.33$) as the propagating medium. The focused reflection matrix is determined over a field-of-view of $153 \times 153 \mu\text{m}$ and a de-scan distance $\Delta\rho = 7.5 \mu\text{m}$. The spatial sampling is $\delta\rho_c = 300 \text{ nm}$ in the transverse direction and $\delta z = 1.5 \mu\text{m}$ along the z -axis.

Reflection point spread functions

To probe the local RPSF, the field-of-view at each depth z into 16×16 regions defined by their central midpoint $\boldsymbol{\rho}_p = (x_p, y_p)$ and of spatial extension $L = 9 \mu\text{m}$. A local average of the back-scattered intensity is then performed in each region:

$$RPSF(\Delta\boldsymbol{\rho}, \boldsymbol{\rho}_p, z) = \langle |R(\boldsymbol{\rho}_{\text{out}}, \boldsymbol{\rho}_{\text{out}} + \Delta\boldsymbol{\rho}, z)|^2 W_L(\boldsymbol{\rho}_{\text{out}} - \boldsymbol{\rho}_p) \rangle_{\boldsymbol{\rho}_{\text{out}}} \quad (2)$$

where the symbol $\langle \dots \rangle_m$ stands for an average over the variable m in subscript. $W_L(\boldsymbol{\rho} - \boldsymbol{\rho}_p) = 1$ for $|x - x_p| < L/2$ and $|y - y_p| < L/2$, and zero otherwise.

Aberration correction process

The aberration correction process has already been described in Ref. [31]. Local input/output aberration phase laws, $\phi_{\text{in/out}}(z) = [\phi_{\text{in/out}}(\mathbf{u}, \boldsymbol{\rho}_p, z)]$, are estimated by considering the pupil correlation between wave distortions exhibited by the incident/reflected wave-fields for the set of virtual detectors/sources contained in each window W_L defined above.

Transmission matrices $\mathbf{G}_{\text{in/out}}$ linking the source/imaging plane ($\boldsymbol{\rho}_{\text{in/out}}$) and each focal plane ($\boldsymbol{\rho}$) of depth z can be deduced from the estimated aberration phase laws $\Phi_{\text{in/out}}$ as follows:

$$\mathbf{G}_{\text{in/out}}(z) = \{\mathbf{P}^T \circ \exp[i\Phi_{\text{in/out}}(z)]\} \times \mathbf{P}^*. \quad (3)$$

where $\mathbf{P} = [P(\mathbf{u}, \boldsymbol{\rho})]$ is the Fourier transform operator, such that $P(\mathbf{u}, \boldsymbol{\rho}) = \exp[i2\pi\mathbf{u} \cdot \boldsymbol{\rho}/(\lambda f)]$, with f the MO focal length. The symbols \circ and \times stands for the Hadamard and matrix product, respectively. The superscripts T and $*$ stand for matrix transposition and conjugation, respectively.

Aberrations are then compensated by applying the phase conjugate of the transmission matrices at the input and output of the focused \mathbf{R} -matrix:

$$\mathbf{R}_{\boldsymbol{\rho}\boldsymbol{\rho}}''(z) = \mathbf{G}_{\text{out}}^\dagger(z) \times \mathbf{R}_{\boldsymbol{\rho}\boldsymbol{\rho}}(z) \times \mathbf{G}_{\text{in}}^*(z) \quad (4)$$

The final image of the sample can be obtained by considering the diagonal elements of the corrected matrix $\mathbf{R}_{\boldsymbol{\rho}\boldsymbol{\rho}}''$:

$$I_M(\boldsymbol{\rho}, z) = R''(\boldsymbol{\rho}, \boldsymbol{\rho}, z). \quad (5)$$

ACKNOWLEDGMENTS

VB, FB, NG, PB and AA are grateful for the funding provided by the European Research Council (ERC) under the European Union's Horizon 2020 research and innovation program (grant agreement no. 819261, REMINISCENCE project). This project has also received funding from Labex WIFI (Laboratory of Excellence within the French Program Investments for the Future; ANR-10-LABX-24 and ANR-10-IDEX-0001-02 PSL*) and from CNRS Innovation (Prematuration program, MATRISCOPE project). VBr, OD, AJ and ABG acknowledge the embryo production facility of the BREED Unit. Their work is funded by the REVIVE Labex (Investissement d'Avenir, ANR-10-LABX-73) and supported by the PHASE Department of the French National Research Institute for Agriculture, Food and Environment (INRAE).

-
- [1] D. K. Gardner, M. Lane, J. Stevens, T. Schlenker, and W. B. Schoolcraft, Blastocyst score affects implantation and pregnancy outcome: Towards a single blastocyst transfer, *Fertility and Sterility* **73**, 1155 (2000).
 - [2] R. Hoffman and L. Gross, Modulation Contrast Microscope, *Applied Optics* **14**, 1169 (1975).
 - [3] V. Barolle, J. Scholler, P. Mécê, J.-M. Chassot, K. Groux, M. Fink, A. C. Boccara, and A. Aubry, Manifestation of aberrations in full-field optical coherence tomography, *Opt. Express* **29**, 22044 (2021).
 - [4] A. Badon, A. C. Boccara, G. Lerosey, M. Fink, and A. Aubry, Multiple scattering limit in optical microscopy, *Opt. Express* **25**, 28914 (2017).
 - [5] A. Domingo-Muelas, R. M. Skory, A. A. Moverley, G. Ardestani, O. Pomp, C. Rubio, P. Tetlak, B. Hernandez, E. A. Rhon-Calderon, L. Navarro-Sánchez, C. M. García-Pascual, S. Bissiere, M. S. Bartolomei, D. Sakkas, C. Simón, and N. Plachta, Human embryo live imaging reveals nuclear DNA shedding during blastocyst expansion and biopsy, *Cell* **186**, 3166 (2023).
 - [6] K. Karnowski, A. Ajduk, B. Wieloch, S. Tamborski, K. Krawiec, M. Wojtkowski, and M. Szkulmowski, Optical coherence microscopy as a novel, non-invasive method for the 4D live imaging of early mammalian embryos, *Scientific Reports* **7**, 4165 (2017).
 - [7] A. Sobkowiak, M. Fluks, E. Kosyl, R. Milewski, M. Szpila, S. Tamborski, M. Szkulmowski, and A. Ajduk, The number of nuclei in compacted embryos, assessed by optical coherence microscopy, is a non-invasive and robust marker of mouse embryo quality, *Molecular Human Reproduction*, gaae012 (2024).
 - [8] S. Morawiec, A. Ajduk, P. Stremplewski, B. F. Kennedy, and M. Szkulmowski, Full-field optical coherence microscopy enables high-resolution label-free imaging of the dynamics of live mouse oocytes and early embryos, *Communications Biology* **7**, 1 (2024).
 - [9] H. W. Babcock, The possibility of compensating astronomical seeing, *Publications of the Astronomical Society of the Pacific* **65**, 229 (1953).
 - [10] A. Labeyrie, Attainment of Diffraction Limited Resolution in Large Telescopes by Fourier Analysing Speckle Patterns in Star Images, *Astronomy and Astrophysics* **6**, 85 (1970).
 - [11] R. A. Muller and A. Buffington, Real-time correction of atmospherically degraded telescope images through image sharpening, *J. Opt. Soc. Am.* **64**, 1200 (1974).
 - [12] F. Roddier, ed., *Adaptive Optics in Astronomy* (Cambridge University Press, Cambridge, 1999).
 - [13] B. Hermann, E. Fernández, A. Unterhuber, H. Sattmann, A. Fercher, W. Drexler, P. Prieto, and P. Artal, Adaptive-optics ultrahigh-resolution optical coherence to-

- mography, *Opt. Lett.* **29**, 2142 (2004).
- [14] M. J. Booth, M. A. Neil, R. Juškaitis, and T. Wilson, Adaptive aberration correction in a confocal microscope, *Proc. Natl. Acad. Sci. U. S. A.* **99**, 5788 (2002).
 - [15] M. J. Booth, Adaptive optical microscopy: The ongoing quest for a perfect image, *Light Sci Appl* **3**, e165 (2014).
 - [16] J.-L. Robert and M. Fink, Green’s function estimation in speckle using the decomposition of the time reversal operator: Application to aberration correction in medical imaging, *J. Acoust. Soc. Am.* **123**, 866 (2008).
 - [17] A. Aubry and A. Derode, Detection and imaging in a random medium : A matrix method to overcome multiple scattering and aberration, *J. Appl. Phys.* **106**, 044903 (2009).
 - [18] S. G. Adie, B. W. Graf, A. Ahmad, P. S. Carney, and S. A. Boppart, Computational adaptive optics for broadband optical interferometric tomography of biological tissue, *Proc. Nat. Acad. Sci. USA* **109**, 7175 (2012).
 - [19] A. Ahmad, N. D. Shemonski, S. G. Adie, H.-S. Kim, W.-M. W. Hwu, P. S. Carney, and S. A. Boppart, Real-time in vivo computed optical interferometric tomography, *Nat. Photonics* **7**, 444 (2013).
 - [20] S. Kang, S. Jeong, W. Choi, H. Ko, T. D. Yang, J. H. Joo, J.-S. Lee, Y.-S. Lim, Q.-H. Park, and W. Choi, Imaging deep within a scattering medium using collective accumulation of single-scattered waves, *Nat. Photonics* **9**, 253 (2015).
 - [21] A. Badon, V. Barolle, K. Irsch, A. C. Boccara, M. Fink, and A. Aubry, Distortion matrix concept for deep optical imaging in scattering media, *Sci. Adv.* **6**, eaay7170 (2020).
 - [22] S. Yoon, M. Kim, M. Jang, Y. Choi, W. Choi, S. Kang, and W. Choi, Deep optical imaging within complex scattering media, *Nat. Rev. Phys.* **2**, 141 (2020).
 - [23] F. Bureau, J. Robin, A. Le Ber, W. Lambert, M. Fink, and A. Aubry, Three-dimensional ultrasound matrix imaging, *Nat. Commun.* **14**, 6793 (2023).
 - [24] S. M. Popoff, A. Aubry, G. Lerosey, M. Fink, A. C. Boccara, and S. Gigan, Exploiting the Time-Reversal Operator for Adaptive Optics, Selective Focusing, and Scattering Pattern Analysis, *Phys. Rev. Lett.* **107**, 263901 (2011).
 - [25] A. Badon, D. Li, G. Lerosey, A. C. Boccara, M. Fink, and A. Aubry, Smart optical coherence tomography for ultra-deep imaging through highly scattering media, *Sci. Adv.* **2**, e1600370 (2016).
 - [26] S. Yoon, H. Lee, J. H. Hong, Y.-S. Lim, and W. Choi, Laser scanning reflection-matrix microscopy for aberration-free imaging through intact mouse skull, *Nat. Commun.* **11**, 5721 (2020).
 - [27] Y. Kwon, J. H. Hong, S. Kang, H. Lee, Y. Jo, K. H. Kim, S. Yoon, and W. Choi, Computational conjugate adaptive optics microscopy for longitudinal through-skull imaging of cortical myelin, *Nat. Commun.* **14**, 105 (2023).
 - [28] Y. Zhang, D. Minh, Z. Wang, T. Zhang, T. Chen, and C. W. Hsu, Deep imaging inside scattering media through virtual spatiotemporal wavefrontshaping,

arXiv:2306.08793 (2023).

- [29] Y.-R. Lee, D.-Y. Kim, Y. Jo, M. Kim, and W. Choi, Exploiting volumetric wave correlation for enhanced depth imaging in scattering medium, *Nat. Commun.* **14** (2023).
- [30] U. Najar, V. Barolle, P. Balondrade, M. Fink, A. C. Boccara, M. Fink, and A. Aubry, Harnessing forward multiple scattering for optical imaging deep inside an opaque medium, *Nat. Commun.* **15**, 7349 (2024).
- [31] P. Balondrade, V. Barolle, N. Guigui, E. Auriant, N. Rougier, C. Boccara, M. Fink, and A. Aubry, Multi-spectral reflection matrix for ultrafast 3D label-free microscopy, *Nat. Photon.* **18**, 1097 (2024).
- [32] T. Chaigne, Revealing the unseeable by digital clearing, *Nature Photonics* **18**, 1006 (2024).
- [33] W. Lambert, L. A. Cobus, M. Couade, M. Fink, and A. Aubry, Reflection matrix approach for quantitative imaging of scattering media, *Physical Review X* **10**, 021048 (2020).
- [34] G. Osnabrugge, R. Horstmeyer, I. N. Papadopoulos, B. Judkewitz, and I. M. Vellekoop, Generalized optical memory effect, *Optica* **4**, 886 (2017).
- [35] H. J. Clarke, Transzonal projections: Essential structures mediating intercellular communication in the mammalian ovarian follicle, *Molecular Reproduction and Development* **89**, 509 (2022).
- [36] B. Tatham, A. Sathananthan, V. Dharmawardena, D. Munasinghe, I. Lewis, and A. Trounson, Fertilization and early embryology: Centrifugation of bovine oocytes for nuclear micromanipulation and sperm microinjection, *Human Reproduction* **11**, 1499 (1996).
- [37] C. Diez, Y. Heyman, D. Le Bourhis, C. Guyader-Joly, J. Degrouard, and J. Renard, Delipidating in vitro-produced bovine zygotes: Effect on further development and consequences for freezability, *Theriogenology* **55**, 923 (2001).
- [38] J. Scholler, K. Groux, O. Goureau, J.-A. Sahel, M. Fink, S. Reichman, C. Boccara, and K. Grieve, Dynamic full-field optical coherence tomography: 3d live-imaging of retinal organoids, *Light Sci. Appl.* **9**, 140 (2020).
- [39] G. Coticchio, C. Lagalla, M. Taggi, D. Cimadomo, and L. Rienzi, Embryo multinucleation: detection, possible origins, and implications for treatment, *Human Reproduction* 10.1093/humrep/deae186 (2024).
- [40] S. Yaacobi-Artzi, D. Kalo, and Z. Roth, Association between the morphokinetics of in-vitro-derived bovine embryos and the transcriptomic profile of the derived blastocysts, *PLOS ONE* **17**, e0276642 (2022).
- [41] B. Gul, S. Ashraf, S. Khan, H. Nisar, and I. Ahmad, Cell refractive index: Models, insights, applications and future perspectives, *Photodiagnosis and Photodynamic Therapy* **33**, 102096 (2021).
- [42] J. R. Mourant, J. P. Freyer, A. H. Hielscher, A. A. Eick, D. Shen, and T. M. Johnson, Mechanisms of light scattering from biological cells relevant to noninvasive

- optical-tissue diagnostics, *Applied Optics* **37**, 3586 (1998).
- [43] F. Magata, Time-lapse monitoring technologies for the selection of bovine in vitro fertilized embryos with high implantation potential, *Journal of Reproduction and Development* **69**, 57 (2023).
 - [44] F. Bureau, E. Giraudat, A. Le Ber, W. Lambert, L. Carmier, A. Guibal, M. Fink, and A. Aubry, Reflection matrix imaging for wave velocity tomography, *arXiv:2409.13901* (2024).
 - [45] P. Stahli, C. Becchetti, N. Korta Martiartu, A. Berzigotti, M. Frenz, and M. Jaeger, First-in-human diagnostic study of hepatic steatosis with computed ultrasound tomography in echo mode, *Communications Medicine* **3**, 176 (2023).
 - [46] A. Goicoechea, C. Brutt, F. Bureau, A. Le Ber, C. Prada, and A. Aubry, Reflection measurement of the scattering mean free path at the onset of multiple scattering, *Phys. Rev. Lett.* (to be published) (2024).